3D Deconvolution Microscopy

David S.C. Biggs[1]

[1]KB Imaging Solutions LLC, Waterford, New York

ABSTRACT

3D deconvolution microscopy is a combination of optical and computational techniques that are used to maximize the observed resolution and signal from a biological specimen. Mathematical models are used to predict the distribution of out-of-focus light caused by the inherent optical limitations of the instrument, which can then be compensated for using computer algorithms. This unit will review the theory of image formation and characteristics of the point spread function (PSF) based on the instrument modality and objective lens parameters. A variety of commonly used deblurring and deconvolution methods are described, and their applications to sample datasets are illustrated to show the performance of each algorithm. Steps for setting up the image acquisition to acquire data suitable for deconvolution are described, and the challenge of maximizing signal levels while minimizing light exposure addressed. Deconvolution examples from widefield epifluorescence and laser scanning confocal are shown, and suitability for other modalities discussed. *Curr. Protoc. Cytom.* 52:12.19.1-12.19.20. © 2010 by John Wiley & Sons, Inc.

Keywords: deconvolution • deblurring • image restoration • point spread function • fluorescence • widefield • confocal

INTRODUCTION

The modern research-grade widefield fluorescence microscope is a marvel of optical engineering, precision manufacturing, and computer automation. However, without a solid understanding of the underlying image formation process there is no way to maximize the performance of the instrument and gather the data necessary to support the research being performed.

There are endless combinations of lenses, filters, cameras, image capture settings, and microscope adjustments possible that can leave users easily confused. However, this can be simplified by understanding how to correctly choose the parameters that will optimize the imaging performance.

When observing a sample through an optical microscope, the image that is formed is not a true representation of the light distribution in the specimen. Instead, the optical characteristics and limitations of the instrument transform the light into an image that can be related back to the true specimen. Understanding the image formation process is critical to properly analyzing the observed data. Deconvolution is a mathematical technique that attempts to create a more accurate representation of the specimen from the observed data, thus aiding subsequent analysis and quantification.

In conducting any imaging study, there are several other important considerations including:

Maximizing the resolution of features visible in the specimen
Maximizing the amount of light collected by the camera or photo detector
Minimizing the effect of the observation on the specimen itself

Current Protocols in Cytometry 12.19.1-12.19.20, April 2010
Published online April 2010 in Wiley Interscience (www.interscience.wiley.com).
DOI: 10.1002/0471142956.cy1219s52

Improving the resolution enables closely spaced features to be more clearly identified, and minimizing the out-of-focus light increases the accuracy of subsequent image analysis, segmentation, and visualization. Collecting more light from the specimen improves the signal-to-noise ratio (SNR) between features of interest and the noise contamination that results from counting photons. A conflicting requirement is to minimize the light exposure to the sample so as to prevent photo-damage to a living biological specimen, and photo-bleaching of the fluorophore that otherwise would limit long-term observation.

In order to properly collect all necessary data about the specimen, there are several concepts, such as image formation, resolution, and sampling that must be understood.

IMAGE FORMATION

Using an epi-fluorescence widefield microscope to observe a specimen reveals the characteristic response of the instrument. As the focal plane is moved through the sample and an image comes into focus, structures will become more distinct and brighter. If the specimen is thin and mounted flat, then a single optical plane will reveal all the features in focus. However, if the specimen is thicker than the depth of field of the objective lens, then no single plane can capture all the features in focus. Multiple optical planes are required to fully capture the specimen, and each image will contain in-focus features from the focal plane, and out-of-focus features from all adjacent planes (Agard, 1984). This creates a "haze" of light contamination that severely reduces the ability to clearly distinguish fine specimen structures.

To understand how to relate the image produced by a widefield microscope to the original specimen, consider how a point source of light is transformed. When in focus, the single point of light will appear as a bright spot and may even reveal faint diffraction rings. The spot will have a size that approximately matches the resolution of the objective lens, even if the underlying point structure has a size that is much smaller (e.g., sub-resolution microsphere or quantum dot). As the focal plane is moved away from the in-focus position, the spot will become a disc that grows in size and becomes dimmer. The defocused image should appear the same whether focusing above or below the spot. If not, then spherical aberration may be present, and will be discussed later. Ideally, the amount of light captured in each plane is the same, but the light is spread out over a larger region as the focus moves away from the source.

Reconstructing a three-dimensional (3D) volume of the imaged point source reveals an hourglass shape. The 3D volume is a function that describes how a point source of light is spread by the instrument—this *point spread function*, or PSF, is a defining characteristic of any microscope and is a critical component of the deconvolution process. The half angle of the conical shape (θ) matches that determined by the numerical aperture (NA) of the objective lens, and the refractive index (*RI*) of the lens immersion medium (as shown in Fig. 12.19.1A):

$$\mathrm{NA} = RI \cdot \sin(\theta)$$

Equation 12.19.1

Figure 12.19.2A shows an axial cross-section through a theoretical widefield PSF (1.4 NA oil lens). The *RI* of typical lens immersion media are given in Table 12.19.1.

How the instrument will transform the light from a real 3D specimen can be predicted using the PSF information. A widefield microscope is a linear system that obeys

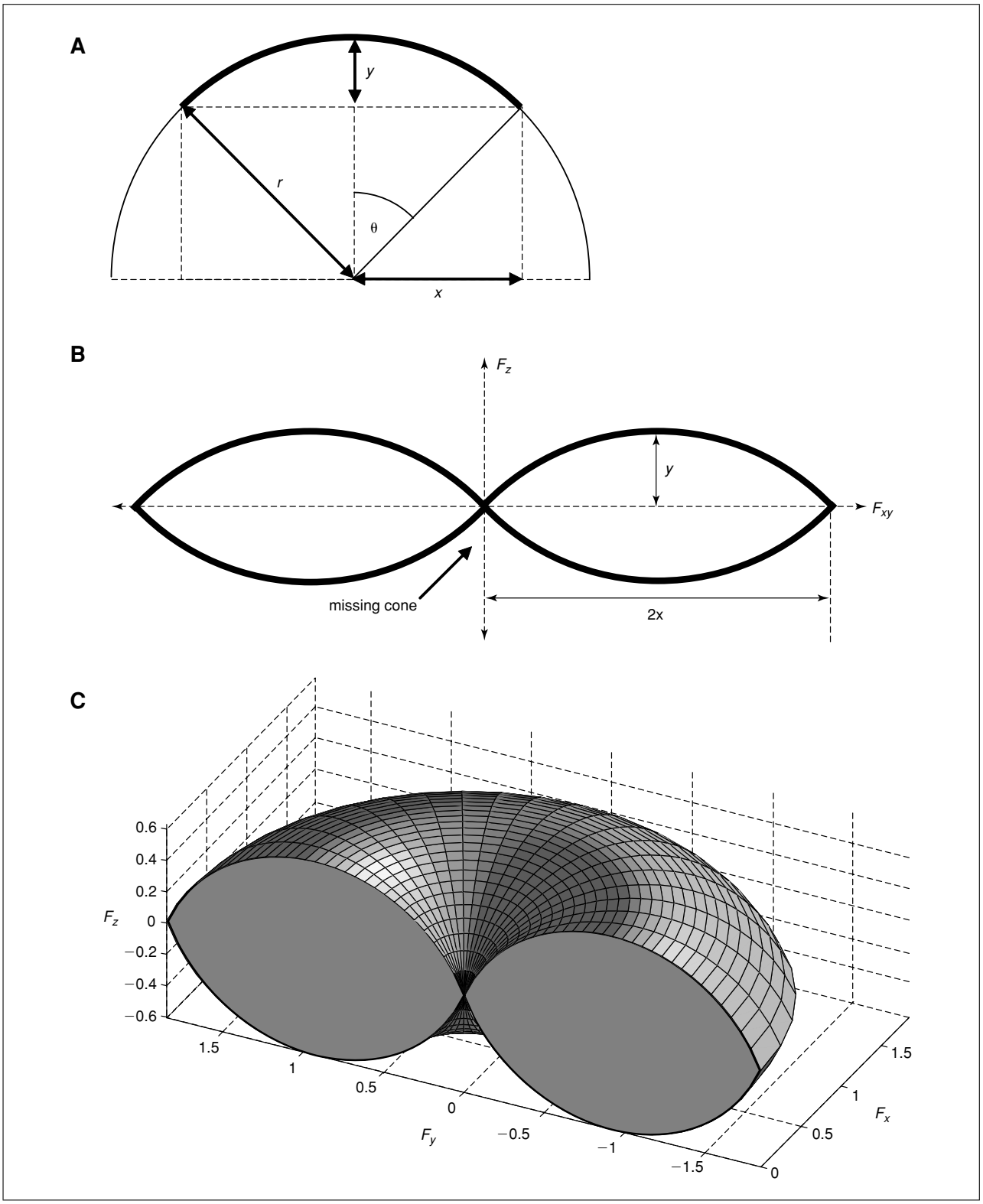

Figure 12.19.1 Calculation of widefield PSF frequency limits. (**A**) Cross-section of the 3D spherical cap that represents the complex pupil function of the objective lens. The numerical aperture (NA) of the lens is defined by the refractive index (*RI*) of the immersion medium, and acceptance half angle (θ). The emission wavelength (λ) then determines the size of the terms *r*, *x*, and *y* as calculated by Equation 12.19.1 and Equation 12.19.2. The observed spatial intensity function is the square of the complex amplitude distribution, which corresponds to the auto-correlation of the spherical cap in the frequency domain. The resulting 3D optical transfer function (OTF) is a 3D toroid with cross-section shown in (**B**). The maximum lateral and axial frequencies are shown, which determine the resolution of the lens. (**C**) Cross-section of toroid that encompasses the 3D OTF of a widefield microscope.

Table 12.19.1 Refractive Index of Typical Objective Lens Immersion Media

Medium	Refractive index
Air	1.0
Water	1.333
Glycerol	1.470
Oil	1.515-1.518

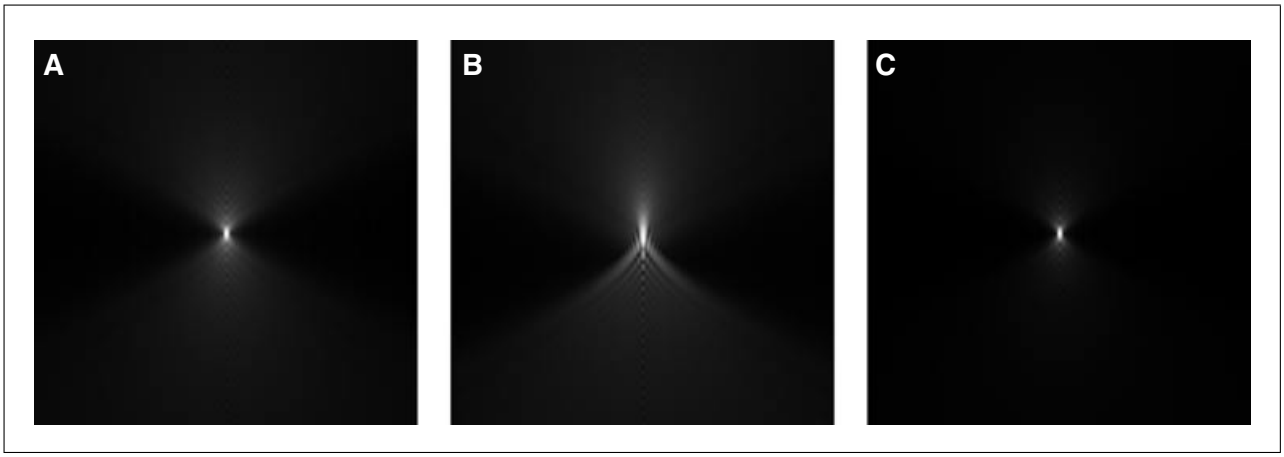

Figure 12.19.2 Axial cross-sections of theoretical calculated PSFs for (**A**) an ideal widefield objective lens (1.4 NA oil at 500nm and no aberrations); (**B**) same lens with 2 waves of negative spherical aberration (peak intensity reduced by half); and (**C**) ideal confocal PSF (square of the widefield PSF). Intensity values displayed with a gamma of 3.

the superposition principle, whereby the total response of a system can be determined by combining the individual responses from all sources. The PSF describes how every point of light from the sample appears to the observer.

A complex 3D specimen can be described as an arrangement of point sources of light, scaled in intensity and positioned throughout a volume. The response of the instrument can then be described by a combination of PSFs scaled in intensity and positioned throughout the volume in the same way as the original specimen. If the PSF is assumed to be the same throughout the volume (spatially invariant), then this process can be described mathematically as a *convolution* between the true data and the PSF. The process to attempt to reverse this effect is therefore termed *deconvolution.*

Point Spread Function (PSF)

The shape and structure of the widefield epi-fluorescence PSF are determined by the optical properties of the objective lens and the wavelength employed. In modeling light propagation through the optical system, it is convenient to consider the shape of the wavefront at the back focal plane of the objective lens. In dealing with high NA objective lenses, it is also more appropriate to consider 3D Fourier optics to properly describe the properties of the PSF (Arnison, 2004).

The shape of the wavefront is modeled as the cap of a sphere as shown in Figure 12.19.1A. The radius of the cap (r), width of the cap (2x), and height of the cap (y) are calculated

using the emission wavelength (λ):

$$r = \frac{RI}{\lambda}$$
$$x = \frac{\mathrm{NA}}{\lambda}$$
$$y = \frac{RI - \sqrt{RI^2 - \mathrm{NA}^2}}{\lambda}$$

Equation 12.19.2

The width and height of the cap are the maximum lateral and axial frequencies, respectively, passed by the optical system.

When the wavefront is imaged to form the PSF, the observed intensity is the squared magnitude of the complex amplitude distribution. By the properties of the Fourier transform, this is equivalent to the auto-correlation of the spherical cap, resulting in a toroid that is the limit of the optical transfer function, or OTF, of the system. The dimensions of the axial cross-section are shown in Figure 12.19.1B, with a 3D view shown in Figure 12.19.1C. The toroid shape illustrates that low frequency axial components are not passed by the widefield system. This is termed the "missing-cone" of frequencies and illustrates why a widefield system may not be well suited to detect a sudden change in fluorescence intensity, such as when imaging thick objects.

In general, the total PSF of the system is a combination of the excitation and emission PSFs. For widefield imaging, the excitation is assumed to be uniform, so that only the emission PSF is considered. For confocal imaging, the excitation and emission PSF are often approximated as being the same, which is then simplified to the square of the emission PSF. The confocal PSF therefore emphasizes the brighter in-focus region, and suppresses the out-of-focus regions, as shown in the theoretical axial cross-section shown in Figure 12.19.2C.

RESOLUTION AND SAMPLING

As shown in the previous section, for a widefield fluorescence microscope, the maximum theoretical optical resolution is determined by NA, *RI*, and λ. The magnification of the lens has no effect on the resolution, and adding additional zoom optics simply results in "empty-magnification" that reveals no additional information about the specimen.

The maximum lateral resolution (R_{XY}) and axial resolution (R_Z) are the inverse of the corresponding maximum OTF frequencies:

$$R_{XY} = \frac{\lambda}{2 \cdot \mathrm{NA}}$$
$$R_Z = \frac{\lambda}{RI - \sqrt{RI^2 - \mathrm{NA}^2}}$$

Equation 12.19.3

For biological specimens this limit is ~200 nm laterally, and 500 nm axially, with a high NA objective lens. The axial resolution is typically three times worse compared to the lateral resolution for a high NA objective lens.

Table 12.19.2 Recommended Lateral (*XY*) and Axial (*Z*) Spacings for Proper Nyquist Sampling of Widefield Fluorescence Data (500-nm Emission Wavelength)[a]

Objective lens	Magnification	NA	RI	*XY* Nyquist	Pixel size	*Z* Nyquist
1.4 NA oil	100	1.40	1.515	89 nm	60 nm	267 nm
1.4 NA oil	60	1.40	1.515	89 nm	100 nm	267 nm
1.2 NA water	60	1.20	1.333	104 nm	100 nm	332 nm
0.95 NA air	40	0.95	1.0	132 nm	150 nm	364 nm
0.75 NA air	20	0.75	1.0	167 nm	300 nm	738 nm
0.45 NA air	10	0.45	1.0	278 nm	600 nm	2337 nm

[a]The image pixel size using 6-μm square camera pixels are also shown, which are well matched to the recommended *XY* Nyquist for high NA objective lenses. Spacings can be increased by up to a factor of 1.5 if required and still be suitable for deconvolution.

The Raleigh resolution criterion is also often used to quantify microscope resolution and describes the minimum distance that two point sources can be separated and still be distinguished. For widefield imaging, this distance is 22% higher than the value calculated from the maximum lateral OTF frequency (Born and Wolf, 1999).

To properly collect all the available information about a specimen, the Nyquist sampling criterion states that the image should be sampled at twice the maximum resolution:

$$S_{XY} = 0.5 \cdot R_{XY} = \frac{\lambda}{4 \cdot \mathrm{NA}}$$
$$S_Z = 0.5 \cdot R_Z = \frac{0.5 \cdot \lambda}{RI - \sqrt{RI^2 - \mathrm{NA}^2}}$$

Equation 12.19.4

For a 1.4 NA oil objective, this translates to approximate spacings of 100 nm in *XY* and 250 nm in *Z*. Table 12.19.2 gives the recommended Nyquist sample spacings (S_{XY} and S_Z) for a variety of objective lenses. The low NA lenses have significantly worse axial resolution compared to the lateral, and are not well suited to accurately reconstruct the full 3D structure of a specimen.

Most scientific-grade CCD cameras have pixels that are typically 6 to 7 μm on each side. When used with a 60× 1.4 NA lens, this conveniently translates to ~100 nm at the specimen. Unless signal levels are unacceptably low, or there is excessive magnification, it is not recommended to use camera binning, as this could cause improper sampling. The image pixel spacing can be estimated by dividing the camera pixel spacing by the total magnification, as shown in Table 12.19.1; however, this should be confirmed using a stage micrometer. For high NA lenses, the camera spacing is usually well matched to the resolution of the objective.

For proper axial sampling, a highly accurate and repeatable focusing mechanism is required, such as a precision Z stepper motor or a piezo-controlled objective lens. Hand-focusing is not accurate enough to produce optical slices that are evenly spaced throughout the sample.

ESTIMATING AND OPTIMIZING THE PSF

The actual PSF of a microscope can be estimated in several ways. One simple method is to calculate the PSF from a theoretical model using the known optical parameters; however, this may not accurately describe the actual optical performance or incorporate all aberrations present.

Another often used approach is to empirically measure the PSF using sub-resolution fluorescent microspheres (100 to 200 nm in diameter) to provide point sources of light. By isolating and imaging individual beads in 3D, and at a variety of wavelengths, a library of PSFs can be built up. This can be a time-consuming task, as a separate bead slide that matches the sample preparation is required, and the beads are often faint and noisy, requiring averaging to produce a suitable dataset. The resulting volume is also often preprocessed further, such as by radial averaging (assuming each slice shows a circularly symmetric diffraction pattern), so as to produce a high-quality PSF that is necessary for accurate deconvolution. If the PSF is not axially symmetric, then spherical aberrations may be present.

Even if an empirical PSF is not collected, a bead slide is very useful in helping to evaluate the optical performance of a microscope. Observing how the individual beads appear, especially when defocused, will help reveal any unwanted aberrations. In particular, the defocused images should be symmetrical above and below the point of focus, and remain circular and centered. Images that show strong rings in one axial direction and haze in the other are typical when spherical aberration is present.

To correct any observed aberrations in the PSF it is necessary to match the sample preparation with the assumptions in the objective lens design. This primarily involves matching the refractive indices of the lens immersion and specimen-embedding medium and ensuring the measured coverslip thickness is 170 nm (no. 1.5 coverslip). When observing a specimen in an aqueous medium, a 1.2 NA water objective will result in a higher effective resolution compared to a 1.4 NA oil immersion objective due to the reduced spherical aberration. When a refractive index mismatch is present, the spherical aberration (SA) typically increases as the focus moves away from the coverslip and deeper into the specimen, reducing the resolution, signal level, and depth penetration. SA is a major factor in limiting the depth penetration of confocal microscopes. Figure 12.19.2B shows the axial cross-section of a calculated PSF with 2 waves of negative spherical aberration present, resulting in strong ringing artifacts below the center, a significantly elongated axial profile, which reduces the height of the axial profile, and a peak intensity half that of the unaberrated PSF shown in Figure 12.19.2A. Since spherical aberration varies with specimen depth it is not spatially invariant, which can complicate subsequent deconvolution.

In addition to matching the refractive indices and choosing an appropriate coverslip thickness, some objective lenses have a correction collar that can be used to correct for spherical aberration. Manually adjusting the collar will cause the plane of focus to move, requiring constant refocusing before judging whether the new setting is an improvement. Reducing the SA present should result in a brighter specimen and more symmetric defocus about the focal plane (though this becomes more difficult to estimate as the specimen becomes thicker).

A third approach is to have the algorithm determine the PSF directly from the observed data itself (this will be discussed in more depth later).

DEBLURRING AND DECONVOLUTION ALGORITHMS

The use of mathematical algorithms to process microscopy images dates back to the beginning of the personal computer revolution, and as such, limitations in processing power and available memory often restricted the size of the datasets and the sophistication of the reconstructions.

One simple deblurring technique for removing out-of-focus blur and haze is the Nearest-Neighbor method, which requires only three optical slices at a time, reducing the memory requirements (Cannell et al., 2006). The two planes adjacent to the slice of interest are blurred and used to estimate the out-of-focus contribution in the slice of interest. Subtracting away a proportion of the estimated blur (typically 90% to 99%) leaves only the in-focus features to remain. The resulting dataset may visually appear to have less haze and blur; however, a large proportion of the collected light is removed and the pixel intensities cannot be quantified. When only a single optical slice is available, the Nearest-Neighbors method is reduced to a No-Neighbors technique, and is equivalent to an unsharp-mask operation that is often used in photography. The neighbor-based deblurring methods are often included in most deconvolution software packages, often for historical purposes or for comparison with more accurate deconvolution algorithms.

While deblurring methods attempt to remove the blur in the images, deconvolution algorithms attempt to reconstruct the true intensity distribution of the specimen from the observed data. The mathematical model for the image formation process in the spatial domain is the true object (f), is convolved with the PSF (h), and contaminated by the noise (n), to give the observed image (g):

$$g = h \otimes f + n$$

Equation 12.19.5

Since the convolution operation ($\otimes$) transforms to a multiplication in the frequency domain, it is often easier to process the data using the Fourier transform operation ($\Im$):

$$G = \Im(g)$$
$$G = H \cdot F + N$$

Equation 12.19.6

Where G, H, F, and N are the Fourier transforms of g, h, f, and n, respectively. The Fourier transform of the PSF, H, is also the OTF.

Ignoring the noise, it may appear that the simplest approach to estimate the true data ($\hat{f}$) is to divide the observed frequency data by the OTF, often referred to as an inverse filter:

$$\hat{f} = \Im^{-1}\left(G \cdot \frac{1}{H}\right)$$

Equation 12.19.7

However, this is rarely possible, because of zeros in the OTF, and the amplification of the broadband noise contamination that overwhelms the result. A more practical method

is the Wiener filter, which takes account of the noise component and weighs the filter based upon the signal-to-noise ratio at each frequency (Gonzalez and Woods, 2007):

$$\hat{f} = \Im^{-1}\left(G \cdot \frac{1}{H} \cdot \frac{|F \cdot H|^2}{|F \cdot H|^2 + |N|^2} \right)$$

Equation 12.19.8

this can be rewritten as:

$$\hat{f} = \Im^{-1}\left(G \cdot \frac{H^*}{|H|^2 + \frac{|N|^2}{|F|^2}} \right)$$

Equation 12.19.9

where H^* is the complex conjugate of H. Since the power spectrum of the true object is generally unknown, the Wiener filter is often simplified to:

$$\hat{f} = \Im^{-1}\left(G \cdot \frac{H^*}{|H|^2 + k} \right)$$

Equation 12.19.10

where the k parameter controls balance between signal amplification and noise suppression.

The Wiener filter is a linear restoration method because it can be applied in a single operation. The filter attempts to directly estimate the true object from the observation. However, the linear filter only enhances frequencies inside the OTF, and has no constraints on negative pixel intensities occurring which are not physically possible. To overcome these limitations it is necessary to use nonlinear iterative algorithms.

Iterative algorithms form an estimate of the true object and use the PSF model to simulate how the image would appear through the instrument, which can then be directly compared to the observed data. An error metric is used to determine the accuracy of the *reblurred* data, and the differences are used to form a more accurate estimate of the true object. This process is repeated for a number of iterations until a suitable result is formed and is illustrated in the block diagram shown in Figure 12.19.3. Applying too many iterations can cause the algorithm to over-fit the observed data and cause noise to appear as a spurious structure.

If the noise contamination is signal-independent and Gaussian distributed, then using a *least squares error* (LSE) is an appropriate metric; however, in widefield fluorescence the noise is generally a result of photon counting and thus is signal-dependent and Poisson distributed. One solution is to use a *maximum likelihood* (ML) approach to find the statistically most likely estimate, given the observed data and the noise model. Finding the maximum likelihood solution can be achieved using *expectation maximization* (EM), which eventually produces the following iterative algorithm:

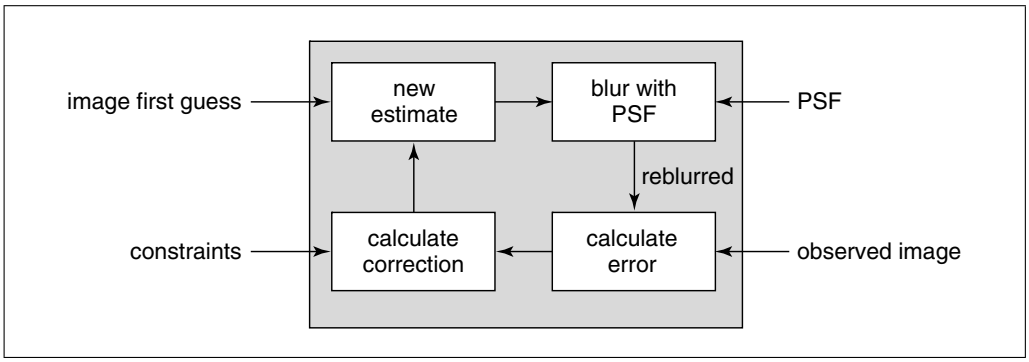

Figure 12.19.3 Block diagram of the iterative deconvolution process. The image estimate is blurred with the PSF to form the reblurred image, which is then compared with the observed image. The image differences and any other constraints are used to form a correction update that creates an improved image estimate. The process is repeated for a number of iterations until a suitable result is achieved.

$$\hat{f}_{k+1} = \hat{f}_k \cdot h * \left(\frac{g}{h \otimes \hat{f}_k} \right)$$

Equation 12.19.11

where $\otimes$ is the convolution operation, and * is the correlation operation. This ML-EM algorithm is often referred to as Richardson-Lucy (RL) iterations (Richardson, 1972; Lucy, 1974) and has several useful characteristics, including guaranteed pixel positivity, stable convergence, and the ability to recover frequency components outside the OTF (which can reduce ringing artifacts that occur at feature edges). The initial estimate used can be just the observed data itself, or the result of another filtering operation, such as the Wiener filter. The closer the estimate is to the solution, the fewer number of iterations required. The standard RL iterations can be slow to converge, so acceleration techniques are normally used to reduce the number of iterations and the amount of processing required. The convolution and correlation operations require a total of four 3D Fourier transform operations per iteration (assuming the PSF is precalculated), which is the bulk of the computations performed.

Another iterative algorithm that is often implemented is Gold's method (Gold, 1964; Sibarita, 2005), which has a similar form to the RL equation; however, it is not a maximum likelihood technique:

$$\hat{f}_{k+1} = \hat{f}_k \cdot \left(\frac{g}{h \otimes \hat{f}_k} \right)$$

Equation 12.19.12

Each iteration requires less computation; however, Gold's method tends to amplify noise, which requires a smoothing operation to be applied at regular intervals (e.g., using a 3D Gaussian filter every three iterations), in order to retain stability.

BLIND DECONVOLUTION

Another method of determining the microscope PSF is to estimate it directly from the observed data itself. The ability to separate the PSF and underlying object from a single observation may, at first, seem counter-intuitive; however, physical constraints such as

pixel positivity and a priori knowledge about the spatial or frequency limits of the PSF enable a suitable solution to be found.

Deconvolving a dataset without direct knowledge of the PSF is referred to as *blind deconvolution*, or using an *adaptive PSF* since the PSF is modified during processing (Biggs, 1998; Holmes et al., 2006). Blind deconvolution techniques usually require additional computational processing; however, they make it quicker and easier for the user because it eliminates the need to empirically measure the PSF for each sample. The optical parameters are still required to form a first estimate of the PSF and to setup any spatial or frequency limits that are imposed on the PSF.

When using standard deconvolution techniques with a fixed PSF, the algorithm will attempt to fit the result to the observation via the PSF model. However, if the provided PSF does not match the actual distortion mechanism, then artifacts such as ringing at edges, removal of actual features, or residual blur can occur, in order for the algorithm to fit the data to the fixed model. In contrast, blind deconvolution allows the algorithm to modify the PSF to better fit the actual data, thus reducing the potential artifacts.

One approach to implementing blind deconvolution uses alternating cycles of the RL algorithm described above. Initially, the PSF is fixed and the image estimate is updated, and then the image is fixed and the PSF estimate updated. This process is repeated, with each cycle making incremental changes to both estimates until they converge to a solution, as shown in Figure 12.19.4. A simple implementation for estimating both the image and PSF (Fish et al., 1995) is:

$$\hat{f}_{k+1} = \hat{f}_k \cdot h_k * \left(\frac{g}{h_k \otimes \hat{f}_k} \right)$$

$$\hat{h}_{k+1} = \hat{h}_k \cdot \hat{f}_{k+1} * \left(\frac{g}{h_k \otimes \hat{f}_{k+1}} \right)$$

Equation 12.19.13

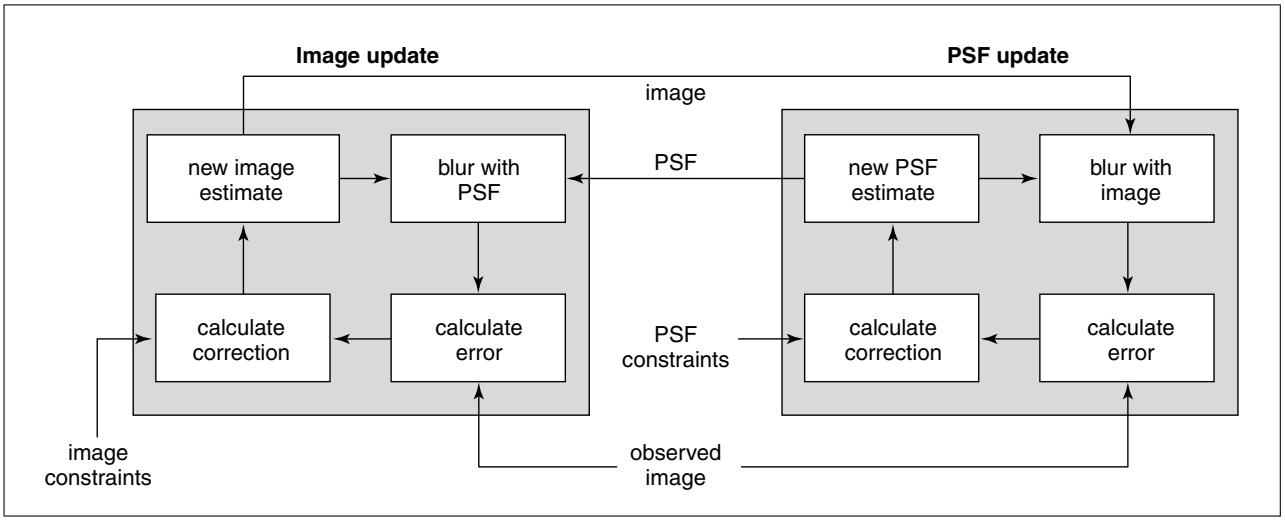

Figure 12.19.4 Block diagram of the iterative blind deconvolution process using alternating update cycles. First, the PSF is fixed and the image is updated, then the image is fixed and the PSF updated. With appropriate starting estimates, constraints, and a priori knowledge, a suitable solution for the image can be found while the PSF is adapted to better fit the data.

EXAMPLE DECONVOLUTION RESULTS

The results from a variety of common deblurring and deconvolution algorithms are shown in Figure 12.19.5. The specimen is a HeLa cell undergoing mitosis and is imaged using widefield epi-fluorescence with four fluorescent probes (DAPI, FITC, Texas Red, and Cy5). A 1.4 NA oil objective lens is used and the data is captured using 640 × 640 pixels with 50 nm spacing and 95 Z slices separated by 200 nm. The volume captured is 32-μm square by 19-μm deep, and the peak intensity for each channel is ∼2000 counts. The original data is courtesy of Jason Swedlow, University of Dundee. All the results were generated using the deconvolution modules available in the cellSens Dimension software from Olympus (Tokyo, Japan). Additional image projection generation was performed using Matlab (Natick, MA).

Lateral (*XY*) and axial (*XZ*) maximum intensity projections for each channel of the original data are shown in Figure 12.19.5A. The Nearest Neighbors (NN) result with 95% setting is shown in Figure 12.19.5B, which has less haze than the original but also has enhanced visible noise. The axial projections also exhibit some intensity flicker that is amplified from what is apparent in the original data. The Wiener filter result shown in Figure 12.19.5C has good noise suppression and clearer feature details, but with some residual haze still visible in the background regions.

Figure 12.19.5D shows results from Gold's method after ten iterations. Gold's method is fast, but requires a smoothing operation to be applied every three iterations in order to retain stability, which reduces the overall resolution improvement. The background blur is well suppressed, but some of the features visible in the original FITC and Texas Red channels appear to have disappeared. Closer inspection reveals that the faint details are present, but overwhelmed by the intensity increase of the brighter point structures. Gold's iterations have a tendency to amplify point-like structures or image defects, which can result in artifacts.

Figure 12.19.5E shows the results after ten iterations of an accelerated MLE-based deconvolution algorithm. This shows high-resolution features and a clean background while retaining faint details. The resolution of restored features is higher than both the Wiener filter and Gold's results. Figure 12.19.5F has the blind deconvolution feature enabled with ten iterations of MLE. In this case, the result is not substantially different from the fixed PSF processing in Figure 12.19.5E, most likely because the theoretical PSF is well matched to what is present in the actual data.

For the iterative MLE algorithms, the total photon count is conserved, but the peak intensity is increased dramatically—by a factor of 5, 39, 37, and 15, for the DAPI, FITC, Texas Red, and Cy5 channels, respectively. Point-like structures in the FITC and Texas Red channels have a much larger increase in peak intensity compared to more uniform structures present in the DAPI channel. The signal level has been increased without requiring longer image exposures. By contrast, the Nearest Neighbors result has the average intensity decreased by 95%, and the peak intensities are reduced by a factor of 3 to 10 times, which is not an effective use of the collected photons.

DECONVOLUTION SOFTWARE

There are a variety of open-source and commercial software packages that can perform deconvolution of 3D optical microscope imagery and can be either built into the acquisition software or be standalone applications. When evaluating how a particular software package performs there are a number of important operations to consider beyond just the quality of the algorithm results, including:

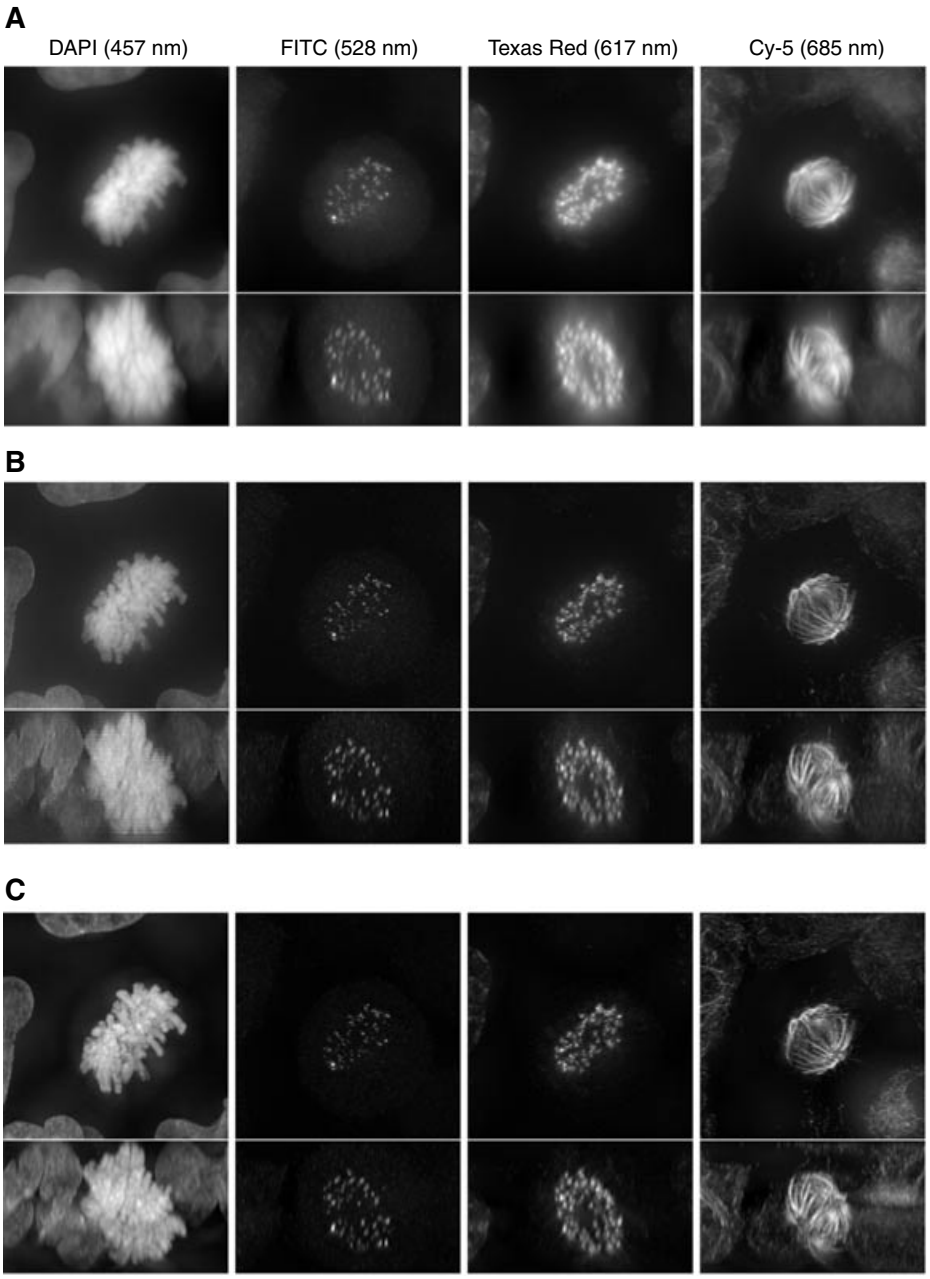

Figure 12.19.5 *(continued on following page)* Maximum intensity *XY* and *XZ* projections of four channels from a HeLa cell undergoing mitosis with results from a variety of deblurring and deconvolutions algorithms. (**A**) Original widefield data, (**B**) Nearest Neighbors at 95% setting, (**C**) Wiener filtering, (**D**) Gold's method with 10 iterations (smoothing every 3 iterations), (**E**) iterative MLE (10 accelerated iterations), and (**F**) blind iterative MLE (10 accelerated iterations). Each volume is 640 $\times$ 640 pixels with 50 nm pixels and 95 *Z*-slices spaced 200 nm apart. *XZ* projections are stretched axially by a factor of 4 to give cubic voxels. Original data is courtesy of Jason Swedlow, University of Dundee.

Reading a variety of image file formats, including native files from the acquisition
Reading image meta-data (e.g., pixel spacings, objective parameters, wavelengths)
Displaying optical slices and 3D projections
Handling multichannel and time-series volumes
Preprocessing the data to correct for illumination non-uniformities or pixel errors
Setting up the parameters for the algorithm

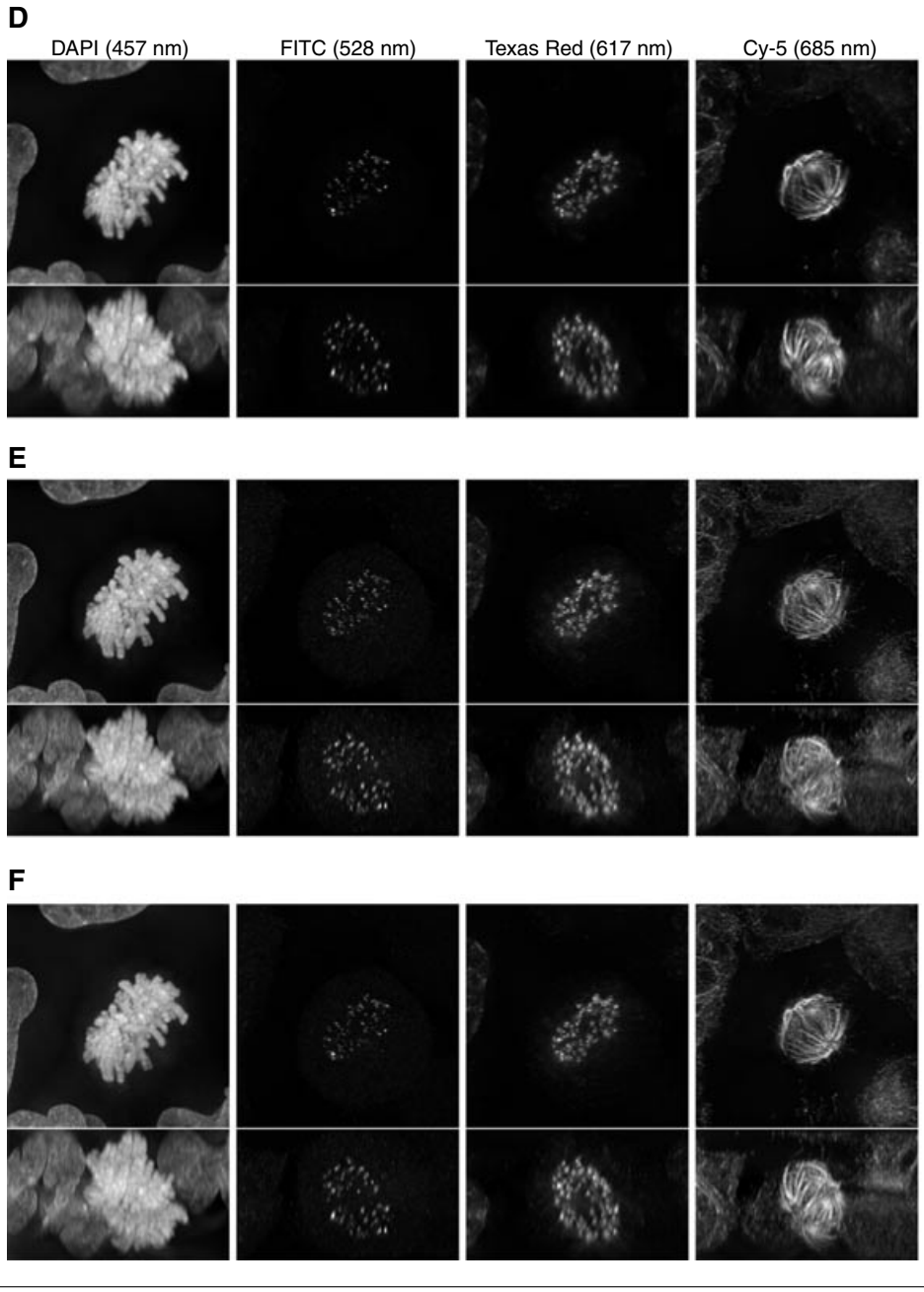

Figure 12.19.5 *(continued)*

Algorithm memory requirements
Limits on size of volume that can be processed
Effective usage of the CPU and multiple processors
Total algorithm processing time
Automated batch processing of multiple datasets
Visualization and comparison of results with the original data
Output of data in format suitable for further analysis

Since deconvolution is an integral part of the imaging process, the workflow from data acquisition to processed results should be as seamless as possible to reduce the amount of manual data handling, such that employing image restoration becomes routine.

Considerations

Always evaluate deconvolution software using actual data collected with the instrument and specimens of interest, and not necessarily with the best signal level possible. Determine the efficiency in terms of user interactions required and computational processing requirements. Software that requires manually entering the optical parameters for each dataset, or that involves constant adjustment of algorithm settings to get a suitable result, is unlikely to result in widespread use by users. It is important that the acquisition software save all the meta-data about the experiment setup in the image file, and that the deconvolution application can read and use this information. The parameters should also be recorded in a laboratory notebook as they can easily be stripped from a file when changing formats. Missing parameter settings is a frequent cause of being unable to properly process a dataset, along with improper sample spacings (e.g., optical slices too far apart).

Confocal and Other Modalities

Deconvolution of widefield microscopy imagery was often seen as competing with laser scanning confocal microscopy since both techniques eliminate a majority of the out-of-focus blur and haze. However, this comparison is not appropriate because each instrument has different strengths when it comes to the type of specimens being imaged, and deconvolution algorithms also can be successfully applied to confocal datasets simply by using an appropriate confocal PSF.

As a broad generalization, widefield epi-fluorescence has a higher light collection efficiency required when imaging faint live specimens, whereas confocal imaging is better for thick tissue where the rejection of out-of-focus light prior to detection is important. In both cases, the choice of instrument should be matched to the type of imaging experiment and specimen.

The confocal PSF is formed by multiplying the light distribution of the excitation PSF with that of the emission PSF, both of which have the form of the regular widefield PSF hourglass shape. Since the excitation and emission wavelengths are normally close, and assuming the detection pinhole is less than 1 Airy disk in diameter, the confocal PSF is often simplified as the square of the emission PSF. This gives a confocal PSF that is shaped like a football/rugby ball and elongated in the axial direction, giving the characteristic axial smearing that occurs with confocal imaging (as shown in Fig. 12.19.2C).

The theoretical highest lateral frequency for the squared confocal PSF is twice that of the widefield PSF; however, the magnitudes are so small that they are difficult to detect and easily contaminated by noise. It is more appropriate to compare the full-width at half-max (FWHM) of the central peak of the PSF, which reveals that the squared confocal PSF has an improved resolution of about 1.4 times that of the widefield PSF. A more accurate confocal PSF model, which includes the effect of the detection pinhole set to 1 Airy disk further reduces the effective lateral confocal resolution to be only fractionally better than the widefield PSF (the resolution is based on the shorter excitation wavelength, rather than the emission wavelength).

Axially the confocal resolution is still ~3 times worse than the lateral resolution; however, the OTF does not exhibit the *missing cone* of frequencies that enables better imaging of thick tissue.

The effect of acquiring data with an appropriate signal-to-noise ratio (SNR) cannot be understated with confocal imaging. Having insufficient light detection by using the smallest confocal pinhole can eliminate any perceived resolution improvement compared to widefield imaging. It is often better to open the pinhole wider and collect more light,

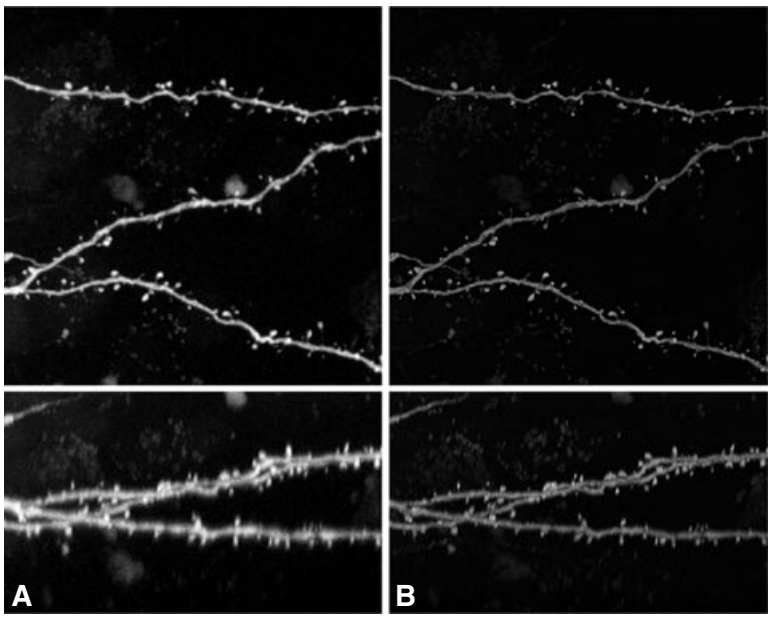

Figure 12.19.6 *XY* and *XZ* maximum intensity projections of neuron sample imaged using a laser scanning confocal microscope. (**A**) Original dataset, and (**B**) following 10 iterations of accelerated MLE deconvolution. The axial smearing inherent with confocal imaging is significantly reduced, resulting in improved axial resolution, and a peak signal intensity that has increased by a factor of 8. The lens used is a 63× 1.4 NA oil objective, and the dye is Alexa 488. The displayed volume is 512 × 512 pixels at 100 nm spacing, and 256 optical slices spaced 118 nm apart. Original data courtesy of Alfredo Rodriguez, Department of Neuroscience, Mount Sinai School of Medicine.

thus raising the SNR, and then compensate for any increased out-of-focus light using deconvolution post-processing. For examples of confocal imaging with larger pinholes followed by deconvolution, see Larson (2002).

Deconvolution of 3D confocal datasets is most effective at minimizing the axial smearing and can also cleanup some of the noise contamination caused by photon-limited imaging. For example, deconvolution of 3D neuron datasets reduces the axial smear, making the neuron cross-sections more circular, increasing the accuracy of subsequent segmentation, volume estimation, and neuron tracing. The noise reduction also makes it easier to distinguish faint dendrites from the background. An example of this is shown in Figure 12.19.6.

Multi-photon imaging can also benefit from deconvolution as the effective PSF has similar characteristics to the confocal PSF. The multi-photon PSF is modeled as the square of a widefield-shaped PSF determined by the excitation wavelength, which is typically in the infrared region, and thus has a lower resolution compared to confocal with the same emission wavelength. There is no pinhole required in multi-photon since the light emission is already contained in a small region.

Spinning disk confocal instruments are another modality that can benefit from deconvolution, and the data is often well suited to processing because the SNR is higher than confocal and the out-of-focus blur is less severe than widefield (see Biggs, 2010 for an example).

Beyond fluorescence, even transmitted light bright-field datasets can be deconvolved by considering light absorption rather than emission (Holmes et al., 2006). Assuming the specimen only absorbs photons, then the image data can be inverted with respect

to the background transmitted light, processed using regular deconvolution and then re-inverted. This approach is not suitable if the specimen is a phase object and creates contrast by interference, since the image formation model is not designed to handle this situation.

Most imaging modalities can benefit from deconvolution processing assuming a suitable model for the PSF is available, and that the data is collected with appropriate sample spacings and signal levels.

DATA ACQUISITION AND DECONVOLUTION ANALYSIS

BASIC PROTOCOL

In order to successfully collect a 3D dataset suitable for deconvolution it is necessary to have the appropriate equipment and the ability to accurately control it via software. When employing widefield epi-fluorescence the following equipment is preferred.

Materials

Research-grade widefield optical microscope (upright or inverted)
Monochrome CCD camera, sensitive to low light fluorescence, cooled, 6 to 7 μm pixels, 12- to16-bit images, sufficient sensor size to cover the desired field of view
Plan apochromat/plan fluorite objective lenses (with correction collar if available)
Motorized *Z*-stage or piezo-electric focusing mechanism with nanometer resolution and repeatability
Uniform fluorescence slide to check illumination uniformity
Stage micrometer to calibrate the pixel spacing from the sample to the camera
Light source with stable emission intensity
Computer-controlled excitation shutter
Filter sets matched to the excitation and emission of the fluorescence involved
Brightfield, phase, or DIC optics for initial specimen observation
Acquisition software to control the microscope, *Z* focusing, camera setup and capture, shutter operation, live preview, automated image capture, and file saving
Multi-spectral sub-resolution fluorescence beads, to check the lateral and axial alignment between multiple wavelengths, and to identify any unwanted aberrations or nonsymmetries in the PSF

NOTE: By their nature, laser scanning confocal instruments are normally already an integrated hardware and software solution suitable for automated 3D acquisition.

Set up of acquisition parameters

1. Based on the emission wavelength and objective lens, confirm the lateral pixel resolution is sufficient. Adjust any camera zoom available if required, and calibrate spacing with stage micrometer.
2. Set the optical slice *Z* spacing based on the recommended Nyquist sampling.
3. Insert the slide into the microscope, use transmitted light to initially find, position, and focus on the specimen. If necessary, use fluorescence sparingly.
4. Identify the top of the specimen and then move far enough above that all features of interest are defocused. Set this position as the top of the dataset to be collected. Repeat with finding the bottom of the specimen and move further below to set the bottom of the volume. Determine the axial depth of the volume and the number of optical slices. Increase the *Z* spacing appropriately if the number of slices is deemed excessive.

5. Focus on the brightest optical slice in the volume to be collected. Adjust the exposure time such that the brightest pixel intensity does not exceed 75% of the full dynamic range of the camera for maximum SNR while preventing any intensity saturation.

   If the specimen is sensitive to light exposure or photo-bleaches quickly, reduce the exposure time such that the main features have intensities from 500 to 1000 counts, increase the Z spacing, and reduce the limits of the volume to minimize the total light exposure. Avoid manually observing the specimen under fluorescence as the automated acquisition will be more efficient. If necessary, collect a quick volume with large spacing and quick exposures, and then refine the final acquisition parameters.

6. For multi-channel acquisition, use the same pixel and slice spacings for each channel based on the shortest wavelength. Set up individual exposure times for each wavelength.

   Multi-channel acquisition requires motorized filter selection and proper optical alignment between wavelengths

7. If using a motorized *Z* stage, collect slices from the bottom up such that the focusing mechanism is working against gravity for best accuracy in spacing.

8. Ensure that all parameters are set correctly, and any unknown values the software cannot determine are entered. Record same parameters in a laboratory notebook.

9. Minimize the stray light in the room, any sources of vibration, and temperature or humidity variation.

10. Start the acquisition process and collect the data volume.

Analyze the acquired data volume

11. Open the dataset and scroll through the *Z* slices from top to bottom.

12. Find the brightest slice and ensure the image intensity scaling is set appropriately.

13. Find the dimmest slice and set the background level so that no data is excluded.

14. Find the most defocused slice (top or bottom) and check that the illumination is uniform.

15. Look for any isolated bright (hot) pixels, or dark (dead) pixels. Use data correction tools to fix problem areas if required.

16. Scroll through the slices and check that there is a smooth transition between features visible from one slice to the next (that no structures suddenly appear or disappear between slices); this confirms that the axial sampling is sufficiently fine.

17. Scroll through the slices and look for any intensity variations or flicker between slices. Take an axial maximum or summed intensity projection. Look for uneven overall illumination between slices as this could be caused by an unstable light source, or inaccurate shutter timing. Confirm that the entire axial extent of the specimen is collected.

Apply the deconvolution algorithm

18. Start the deconvolution application/module and load the dataset.

19. Confirm all the image and experiment parameters have been transferred correctly.

20. Crop the image to include just the areas of interest, but leave a sufficient border to include out-of-focus light from the specimen.

21. Select the deconvolution algorithm based on how the results will be used. For a quick impression of the specimen, use deblurring methods or Wiener filtering. If using the results in future analysis or visualization, use an iterative algorithm.

22. Close any unnecessary applications to free available memory and start the algorithm.

Analyze the results

23. Open the deconvolved results and scroll through the slices.
24. Find the brightest slice and ensure the image intensity scaling is set the same for all slices.
25. Find the dimmest slice and set the background level so that no data is excluded.
26. Compare the same slice in the original and deconvolved datasets and confirm that features visible in the restored result are also visible in the original data, and vice-versa. Out-of-focus features should now be contained to the appropriate regions.
27. If noise in the original data now appears as fine "structure" in the result, then too much processing has been performed, and the algorithm has over-fit the data. Adjust the algorithm parameters accordingly (e.g., reduce the number of iterations).
28. If there appears to be any residual haze, then more iterations may be required, or the PSF used may not match what is actually present in the dataset due to additional aberrations or incorrect parameters.
29. Residual haze that appears in only one axial direction is likely an indicator of spherical aberration.
30. Look for any algorithm-generated artifacts such as grid lines that may be the result of sub-volume processing, or boundary effects.
31. Create maximum intensity projections of both the original and deconvolved datasets and compare the blur removal and contrast improvement. Create lateral and axial projections or use 3D volume visualization to explore the datasets.
32. Compare the peak intensity of the deconvolved data compared to the original data. If the deconvolved peak intensity is 65535, then the result may have been converted to 16-bit and the data clipped or scaled, which may limit the ability to quantitatively compare intensities between volumes.

CONCLUDING REMARKS

The application of deconvolution processing to 3D fluorescence data collected from optical microscopes is an essential part of the entire imaging process. Deconvolution is designed to compensate for the inherent optical limitations of the imaging instrument. The requirements on the imaging setup and acquisition parameters for successful deconvolution are the same for proper imaging in the first place. Modern computational processing power and memory availability means that running the algorithms is no longer a rate-limiting step in the experimental process, and the software applications are now user-friendly even to the novice user.

Data from modalities such as widefield, brightfield, confocal, multi-photon, and spinning disk, can all benefit from deconvolution processing. It should be noted that the use of deconvolution is not a substitute for a properly setup instrument and careful data capture. Deconvolution will not make bad data good, it will make good data better. Minimizing aberrations, particularly spherical aberration, is essential to maximizing the quality of the images from the specimen. Deconvolution can help reveal problems with the data acquisition that were otherwise obscured by the out-of-focus light.

Using an appropriate deconvolution algorithm, with the correct PSF, will produce a result that has increased resolution, contrast, and dynamic range, which will then improve the accuracy of subsequent image analysis, segmentation, and visualization.

LITERATURE CITED

Agard, D.A. 1984. Optical sectioning microscopy: Cellular architecture in three dimensions. *Annu. Rev. Biophys. Bioeng.* 13:191-219.

Arnison, M.R. 2004. Phase Control and Measurement in Digital Microscopy. Ph.D. Thesis, University of Sydney, Australia.

Biggs, D.S.C. 1998. Accelerated Iterative Blind Deconvolution. Ph.D. Thesis, University of Auckland, New Zealand. *http://researchspace.auckland.ac.nz/handle/2292/1760*.

Biggs, D.S.C. 2010. A practical guide to deconvolution of fluorescence microscope imagery. *Microscopy Today* 18, No. 1.

Born, M. and Wolf, E. 1999. Principles of Optics, 7th edition. Cambridge University Press. Cambridge.

Cannell, M.B., McMorland, A., and Soeller, C. 2006. Image enhancement by deconvolution. *In* Handbook of Biological Confocal Microscopy, 3rd ed. (J. Pawley, ed.) pp. 488-500. Springer, New York.

Fish, D.A., Brinicombe, A.M., Pike, E.R., and Walker, J.G. 1995. Blind deconvolution by means of the Richardson-Lucy algorithm. *J. Opt. Soc. Am. A* 12:58-65.

Gold, R. 1964. An Iterative Unfolding Method for Matrices, Tech. Rep. ANL-6984. Argonne National Laboratory, Argonne, Illinois.

Gonzalez, R.C. and Woods, R.E. 2007. Digital Image Processing, Prentice Hall, Upper Saddle River, N.J.

Holmes, T.J., Biggs, D., and Abu-Tarif, A. 2006. Blind deconvolution. *In* Handbook of Biological Confocal Microscopy, 3rd ed. (J. Pawley, ed.) pp. 468-487. Springer, New York.

Larson, J. 2002. Two-dimensional and three-dimensional blind deconvolution of fluorescence confocal images. *Proc. SPIE* 86:4621.

Lucy, L.B. 1974. An iterative technique for the rectification of observed distributions. *Astron. J.* 79:745-754.

Richardson, W.H. 1972. Bayesian-based iterative method of image restoration. *J. Opt. Soc. Am.* 62:55-59.

Sibarita, J.B. 2005. Deconvolution microscopy. *Adv. Biochem. Engin./Biotechnol.* 95:201-243.

KEY REFERENCES

To probe further into deconvolution algorithms or understand more about how to get the most out of your microscope imaging, the following sources are recommended:

For short overview articles on deconvolution and microscopy:

Biggs, D.S.C. 2004. Clearing up deconvolution. *Biophotonics Int.* February:32-37.

For a more in-depth review of deconvolution techniques:

Wallace, W., Schaefer, L.H., and Swedlow, J.R. 2001. Working person's guide to deconvolution in light microscopy. *BioTechniques* 31:1076-1097.

Sibarita, 2005. See above.

Holmes, et al., 2006. See above.

For a more technical review of deconvolution algorithms:

Sarder, P. and Nehorai, A. 2006. Deconvolution methods for 3D fluorescence microscopy images: An overview. *IEEE Signal Proc. Mag.* 23:32-45.

For a comprehensive reference book on biological confocal (and widefield) microscopy:

Pawley, J.B. (ed.) 2006. Handbook of Biological Confocal Microscopy, 3rd ed. Springer, New York.

INTERNET RESOURCES

http://micro.magnet.fsu.edu/

An easily accessible reference to microscopy principles, usage and applications can be found at the Molecular Expressions Web site.

http://micro.magnet.fsu.edu/primer/digitalimaging/deconvolution/deconvolutionhome.html

Deconvolution section at Molecular Expressions.

http://www.3ddeconvolution.com/

A tutorial Web site for 3D deconvolution that extends the work presented in this unit, and includes more example results.